



HAL
open science

Regioisomers of organic semiconducting dumbbell-shaped molecules: synthesis and structure-properties relationship

Chaima Mahmoudi, Ibrahim Bulut, Jiang Jing, Sadiara Fall, Benoît Heinrich, Stéphane Méry, Thomas Heiser, Patrick Lévêque, Emilie Steveler, Mustapha Majdoub, et al.

► To cite this version:

Chaima Mahmoudi, Ibrahim Bulut, Jiang Jing, Sadiara Fall, Benoît Heinrich, et al.. Regioisomers of organic semiconducting dumbbell-shaped molecules: synthesis and structure-properties relationship. *European Journal of Organic Chemistry*, 2021, 2021 (22), pp.3170-3177. 10.1002/ejoc.202100473 . hal-03405458

HAL Id: hal-03405458

<https://cnrs.hal.science/hal-03405458>

Submitted on 27 Oct 2021

HAL is a multi-disciplinary open access archive for the deposit and dissemination of scientific research documents, whether they are published or not. The documents may come from teaching and research institutions in France or abroad, or from public or private research centers.

L'archive ouverte pluridisciplinaire **HAL**, est destinée au dépôt et à la diffusion de documents scientifiques de niveau recherche, publiés ou non, émanant des établissements d'enseignement et de recherche français ou étrangers, des laboratoires publics ou privés.

Regioisomers of organic semiconducting dumbbell-shaped molecules: synthesis and structure-properties relationship

Chaima Mahmoudi,^[a,b] Ibrahim Bulut,^[a] Jiang Jing,^[c] Sadiara Fall,^[c] Benoît Heinrich,^[d] Stéphane Méry,^[d] Thomas Heiser,^[c] Patrick Lévêque,^[c] Emilie Steveler,^[e] Mustapha Majdoub,^[b] Nicolas Leclerc*^[a]

[a] C. Mahmoudi, Dr. I. Bulut, Dr. N. Leclerc

Institut de Chimie et Procédés pour l'Énergie, l'Environnement et la Santé (ICPEES), UMR 7515-CNRS, Université de Strasbourg, ECPM, 25 rue Becquerel, 67087 Strasbourg, France. E-mail: leclercn@unistra.fr

[b] C. Mahmoudi, Dr. M. Majdoub

Laboratoire des Interfaces et Matériaux Avancés (LIMA), Faculté des Sciences de Monastir (Université de Monastir), Bd. De l'Environnement, 5019 Monastir, Tunisia.

[c] Dr. S. Fall, Dr. T. Heiser, Dr. P. Lévêque

Laboratoire ICube, UMR 7357-CNRS, Université de Strasbourg, 23 rue du Loess, 67037 Strasbourg, France.

[d] Dr. B. Heinrich, S. Méry

Institut de Physique et de Chimie des Matériaux de Strasbourg (IPCMS), UMR 7504-CNRS, Université de Strasbourg, 23 rue du Loess, 67034 Strasbourg, France.

[e] Dr. E. Steveler

Laboratoire ICube, UMR 7357-CNRS, INSA Strasbourg, 24 Boulevard de la victoire, 67084 Strasbourg Cedex, France.

Abstract

Two new dumbbell-shaped molecules based on two solubilizing and structuring triazatruxene (TAT) units linked by a central chromophore were synthesized and studied. The central chromophore was an electro-deficient fluorene-malononitrile (FM) unit, that can be functionalized symmetrically on two different positions, giving rise to two positional isomers, called TAT-*p*FM and TAT-*m*FM, when the TATs are connected to the 2,7- and 3,6-positions, respectively. The two isomers exhibited different electronic conjugation pathways that drastically affect their absorption properties and energy levels. Moreover, while TAT-*p*FM was organized in a stable 3D mesomorphic structure from room-temperature to the melting, TAT-*m*FM remained crystalline and decomposed before melting. Finally, despite a lower hole mobility, the TAT-*m*FM exhibited the highest Power Conversion Efficiency (PCE) of about 2% in organic solar cells. This higher PCE was attributed essentially to the pronounced internal charge transfer band contribution to the charge photogeneration observed in TAT-*m*FM solar cells.

Introduction

Organic semiconducting (OSC) materials have experienced a dramatic increase of interest in the last three decades thanks to their many interesting properties for optoelectronic applications.^[1-4] Several hundreds of articles are published every year that describe the design, synthesis and characterization of new OSC small molecules and polymers. Considering the enormous impact of electronic conjugation and self-assembly features on the optoelectronic properties of these solid-state materials, it is obvious that regioisomers of

a same molecular structure are likely to exhibit very different properties. Surprisingly, so far, the impact of regioisomers on the OSC material properties has not been much addressed as compared to other (macro-)molecular architectural features. Regioisomers arise essentially from variations in the conjugated backbone or in the side chains. Regarding the latter, by way of example, Lincker *et al.* reported the influence of the side-chains grafting positions on thiophene units used as end-capper of liquid crystalline small molecules.^[5] They clearly highlighted that both molecules exhibit different polymorphisms and charge transport properties, with a significant increase of the hole mobility (as measured by organic field-effect transistor (OFET)) for the regioisomer exhibiting the largest number of structural phases. Concerning the isomers of conjugated backbone, the regioisomers essentially arise from a variation of the bond positions between aromatic units, of the location of the heteroatoms in the conjugated core and of the sequence of aromatic units in extended fused-ring building blocks. Spirobifluorene (SBF) is a chemical structure known to afford several regioisomers.^[6, 6'] In particular, some publications have reported the study of the regioisomers resulting from the ortho or para linkage between the SBF unit and the conjugated backbone. Thus, Bulut *et al.* reported the two regioisomers with the SBF used as end-capper,^[7] while Yang *et al.* implemented the SBF unit as a conjugated bridge between two perylene diimide (PDI) units.^[8] In both cases, the solid-state structures and optoelectronic properties are significantly changed from one isomer to the other, resulting in substantially different device performance. Finally, very few examples have been reported studying the influence of the different isomeric structures on the solid-state structures and optoelectronic properties of more or less fused extended conjugated molecules.^[9-11] One can cite the recent work reported by Jia *et al.* that describes the synthesis and study of three isomers leading to new extended fused-ring non-fullerene acceptor (NFA) molecules.^[12] By resolving the single crystal structure of the three isomers, the authors noticed a huge difference in the solid-state packing arrangement, as one isomer gives a triangular arrangement, the second one an interlinking shackle pattern and the third one exhibits a linear head-to-tail stacking. Combined with slight variations in the energy levels, the best power conversion efficiencies (PCEs) of these NFAs range from 9 to 12%, considering the same electron-donor polymer.

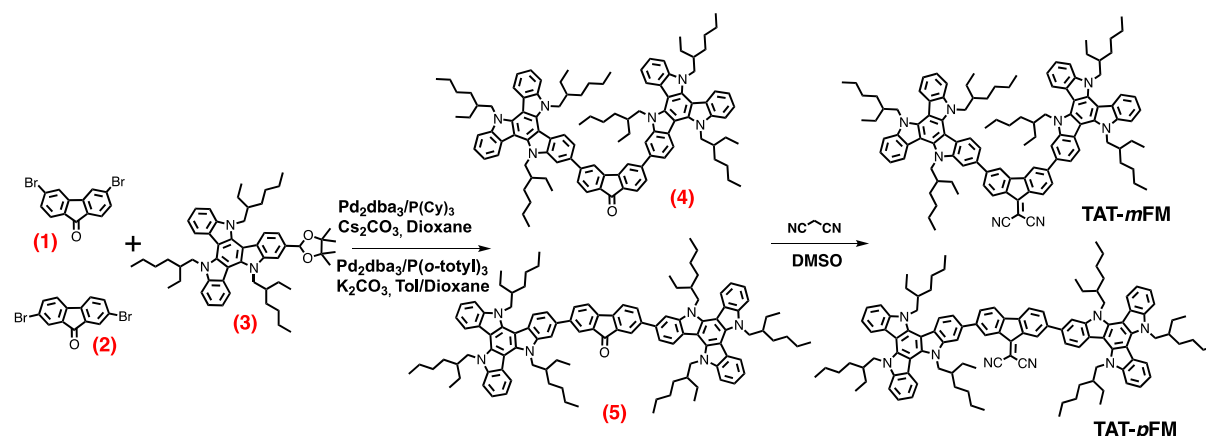
Recently, we reported a new family of solution processable OSC molecules based on the use of the planar triazatruxene (TAT) unit. This family of materials is characterized by its dumbbell shape with two TAT units bridged together by an elongated π -conjugated core, also called central dye. We highlighted that the TAT units act as structuration platforms in thin films while the optoelectronic properties are mainly driven by the central dye composition.^[13] Therefore, by adjusting the nature of the central dye and the solubilizing side chains grafted on the TAT, allows a fine tuning of the optical parameters and energy levels on one side, and of the self-assembling properties on the other side. This two-level fine-tuning enabled at the end to achieve high charge transport and/or photovoltaic performances.^[14-16]

Herein, we report new TAT-based dumbbell-shaped molecules, containing a 9-(dicyanomethylene)fluorene electron deficient central unit. Two regioisomers of this molecule could be produced by connecting the TAT units to the 3,6- or 2,7 positions of the fluorene-malonitrile (FM) core. These two molecules are found to show large variations in physico-chemical and optoelectronic properties that can be explained by the different conjugation pathways (through the meta- or para-linkage), as well as quite different solid-state structures.

Results and Discussion

The synthesis strategy of both TAT-*m*FM and TAT-*p*FM is illustrated in Scheme 1. Synthetic procedure details can be found in the experimental section. 3,6-dibromofluorenone and 2,7-dibromofluorenone have been synthesized by following procedures reported in the literature.^[17,18] The 2-tetramethyldioxaborolane TAT has been functionalized with ramified 2-ethylhexyl side-chains in order to ensure enough solubility to the final compounds. It has been synthesized by following an already reported procedure.^[15]

Both molecules have been obtained through a Suzuki–Miyaura cross-coupling between the monoboronated triazatruxene moiety and the corresponding dibromofluorenone units, followed by a Knoevenagel condensation between the ketone groups (compounds 1 and 2) and an excess of malononitrile.^[19] All compounds were characterized by standard NMR spectroscopy. However, despite the use of ramified side chains on the TAT units, both final molecules are poorly soluble in organic solvents, in particular at room temperature. Consequently, if ¹H NMR at high temperature gave nice resolved spectra, it has not been possible to record readable ¹³C NMR spectra. Therefore MALDI-TOF spectrometry has been used to confirm the final molecules.



Scheme 1. Synthetic routes towards the preparation of TAT-based dyes.

DFT and TD-DFT calculations have been performed, using Gaussian 09 software, in order to support the experimental characterizations. Details regarding calculation methods and functional used can be found in the Supporting information.

A first geometry optimization has been performed through the minimization of energy (Table S1 and S2). Interestingly, both molecules adopt a *cis-cis* geometry (see Figure S1 in SI) in which both dihedral angles, between the central FM unit and the TAT moieties, are equivalent and minimum, ca. around 32-35°.

The electrochemical properties of TAT-*m*FM and TAT-*p*FM have been investigated by cyclic voltammetry (CV) in CH₂Cl₂ (Figure 1). Potentials are given versus a saturated calomel electrode (SCE). The ionization potentials (IP or HOMO level) and electron affinities (EA or LUMO level) were calculated using the following formulas: EA(eV) = E_{onset}^{red} + 4.4; IP(eV) = E_{onset}^{ox} + 4.4. These formulas are based on the assumptions that the energy level of SCE relative to vacuum is 4.4 eV as suggested by Jenekhe and coworkers.^[20] Ferrocene was used as internal reference for calibration. The voltammograms display several well-defined and reversible waves, which can be assigned, by comparison with reference to isolated synthons, to the constitutive molecular fragments of the compounds.

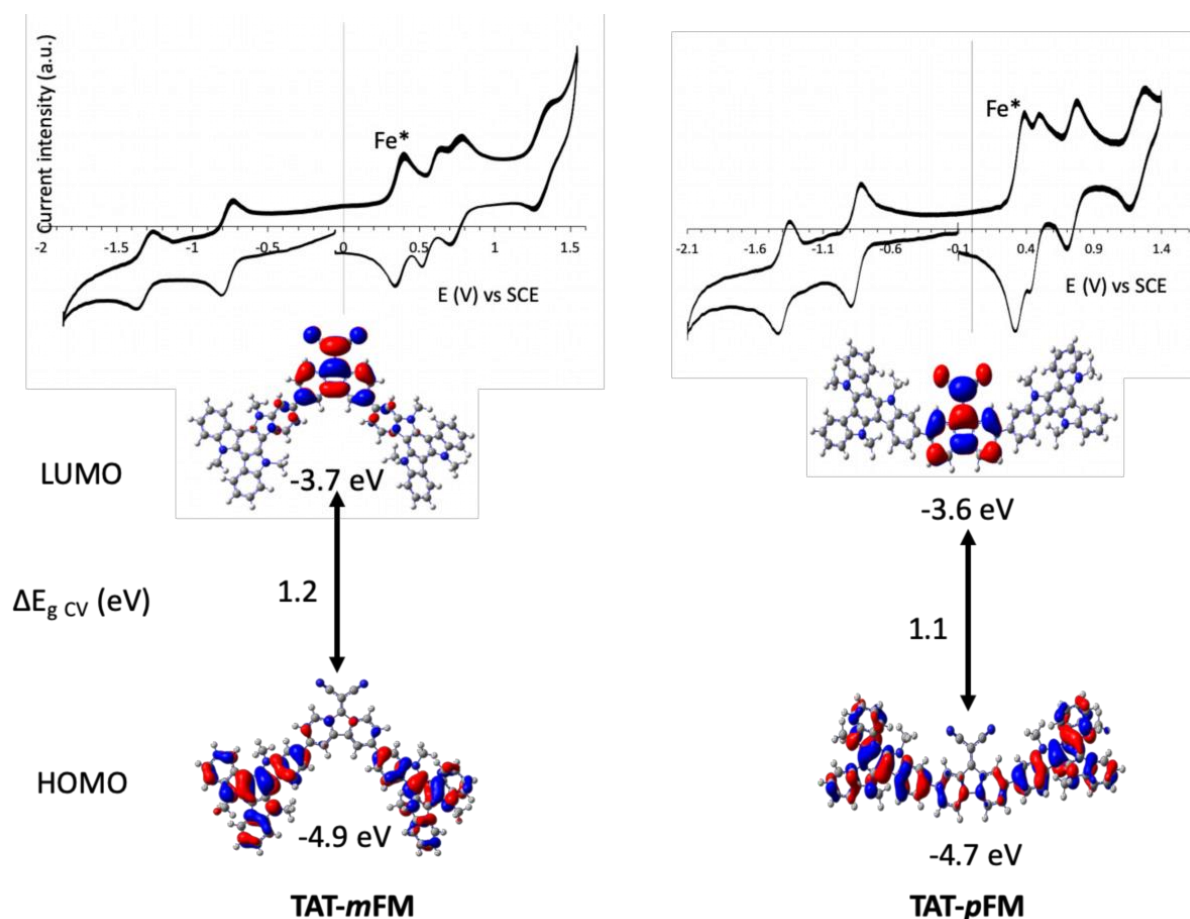


Figure 1. Top. Cyclic voltammograms of **TAT-*m*FM** (left) and **TAT-*p*FM** (right) ($\text{CH}_2\text{Cl}_2 + \text{Bu}_4\text{NPF}_6$ 0.2 M); Sweep-rate: $150 \text{ mV}\cdot\text{s}^{-1}$, platinum wire working electrode). Fe^* corresponds to the redox wave of ferrocene. Bottom. Frontier molecular orbitals LUMO and HOMO and CV extracted energy levels for **TAT-*m*FM** (left) and **TAT-*p*FM** (right).

As previously observed, the TAT fragment is not electroactive in the anodic window, whereas the central FM moiety display two reversible monoelectronic reduction waves, corresponding to the reduction of each nitrile group, as seen usually in other 9-(dicyanomethylene)fluorene derivatives.^[21] The **TAT-*m*FM** exhibits positively shifted reduction processes as compared to the **TAT-*p*FM** derivative, leading to a slightly stabilized EA of -3.7 eV vs -3.6 eV, respectively.

In oxidation, both compounds exhibit three reversible monoelectronic waves, in agreement with previous reported results.^[14] Similarly to the cathodic processes, the **TAT-*m*FM** exhibits positively shifted oxidation processes as compared to the **TAT-*p*FM** derivative. Consequently, HOMO levels are calculated at -4.9 and -4.7 eV for **TAT-*m*FM** and **TAT-*p*FM**, respectively. The slightly larger difference between the HOMO levels, compared to the LUMO levels, can be explained in part by the large difference in electronic delocalization of each HOMO and LUMO level, as calculated by TD-DFT (Figure 1 bottom). Indeed, in the **TAT-*p*FM** molecule, thanks to the para-linkage, the HOMO is fully delocalized on the overall molecule (although the electron density is higher on TAT units), while in the **TAT-*m*FM**, the HOMO level is almost entirely distributed on the TAT units only. In contrast, the LUMO level is in both cases, mainly centered on the FM unit.

UV-visible absorption has been performed in chlorobenzene (CB) solution and as thin-films. The absorption spectra are given in Figures 2 and 3, and the peak maxima of the energy transitions are reported in Table 1.

Table 1. Electrochemical and optical parameters of **TAT-mFM** and **TAT-pFM**.

	E_{ox} (V) [HOMO (eV)]	E_{red} (V) [LUMO (eV)]	λ_{max} [λ_{onset}] (nm)		$E_{\text{g-opt}}$ (eV)	ϵ_{max} ($10^3 \text{ M}^{-1} \cdot \text{cm}^{-1}$) [ϵ_{ICT}]
			Solution	Film		
TAT-mFM	0.52 ; 0.70 ; 1.19 [-4.9]	-0.69 ; -1.23 [-3.7]	Solution	326 ; 364 ; 589 [725]	1.71	140 [27]
			Film	323 ; 364 ; 581 [770]	1.61	
TAT-pFM	0.33 ; 0.61 ; 1.10 [-4.7]	-0.78 ; -1.32 [-3.6]	Solution	320 ; 395 ; 665 [780]	1.57	158 [3.7]
			Film	322 ; 399 ; 640 [890]	1.39	

In solution, the absorption spectra of the two molecules display three maxima. Two of them are located below 450 nm and the third one appears between 500 and 800 nm. Thanks to TD-DFT calculations, the transitions associated to the different bands can be attributed.

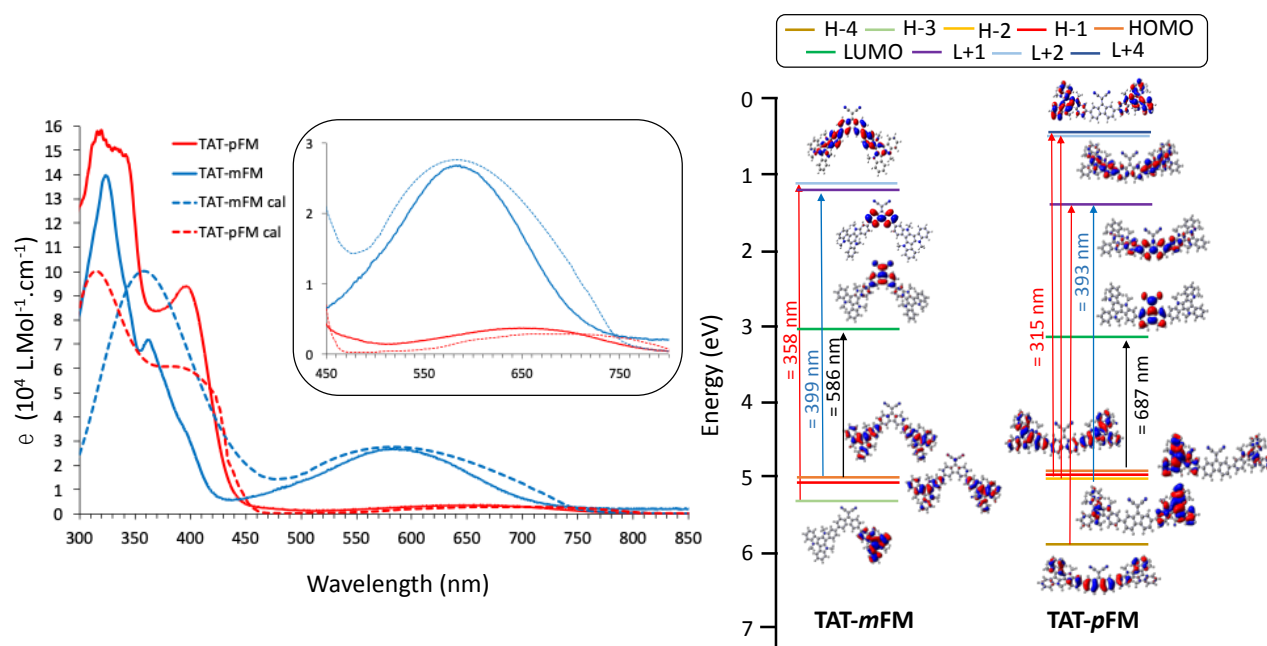


Figure 2. Left. UV-vis absorption spectra in CB solution (full line) and calculated (dashed line) of **TAT-mFM** (blue) and **TAT-pFM** (red). Inset. Zoom on the ICT bands. Right. Representation of the energy levels and the main molecular orbitals involved in the electronic transitions of **TAT-mFM** and **TAT-pFM**.

For **TAT-mFM**, the calculated UV-visible spectrum exhibits only two bands, but the first one results from the merging of the two first bands displayed in the experimental spectrum (see Table S3 reporting the calculated optical transitions for each compounds). Thus, the first high energy band, centered around 325 nm, can be mainly attributed to a transition from the HOMO-3 localized on the TAT units to the LUMO+2 localized on the full molecule. The second band, centered on 375 nm, is mainly assigned to a charge transfer transition from the HOMO orbital localized on the TAT units to the LUMO+1 level localized mainly on the FM group. Finally, the band at higher wavelength with a maximum at 590 nm, corresponds to an

ICT transition between the HOMO and LUMO levels. It is worth noting that this low energy ICT band is relatively intense, as it exhibits an extinction coefficient of $2.7 \cdot 10^4 \text{ M}^{-1} \cdot \text{cm}^{-1}$. This transition is geometrically favored by the fact that the dicyanomethylene group is located in para position from the TAT unit substitutions, leading to an efficient conjugation between the TAT electron donating groups and the electron deficient dicyanomethylene fragment. In contrast, for TAT-*p*FM which also displays three bands, the ICT transition exhibits a very low intensity with a molar extinction coefficient limited to $3750 \text{ M}^{-1} \cdot \text{cm}^{-1}$. This ICT band is also significantly shifted towards longer wavelengths, the maximum being around 655 nm. The very low intensity of this band is explained by the TAT substitution in meta position as regards to the dicyanomethylene unit, greatly reducing the conjugation between electron rich and electron poor fragments. This meta substitution however, leads to an extension of the electronic conjugation between the TAT units through the fluorene core, which translates into the overall bathochromic shift of the bands. The first bands at lower wavelengths are attributed to several transitions between energy levels of type HOMO-1 and HOMO-2 to excited energy levels above the LUMO (see Table S3). The transition centered at 400 nm corresponds mostly to a π - π^* transition between HOMO-2 and LUMO+1.

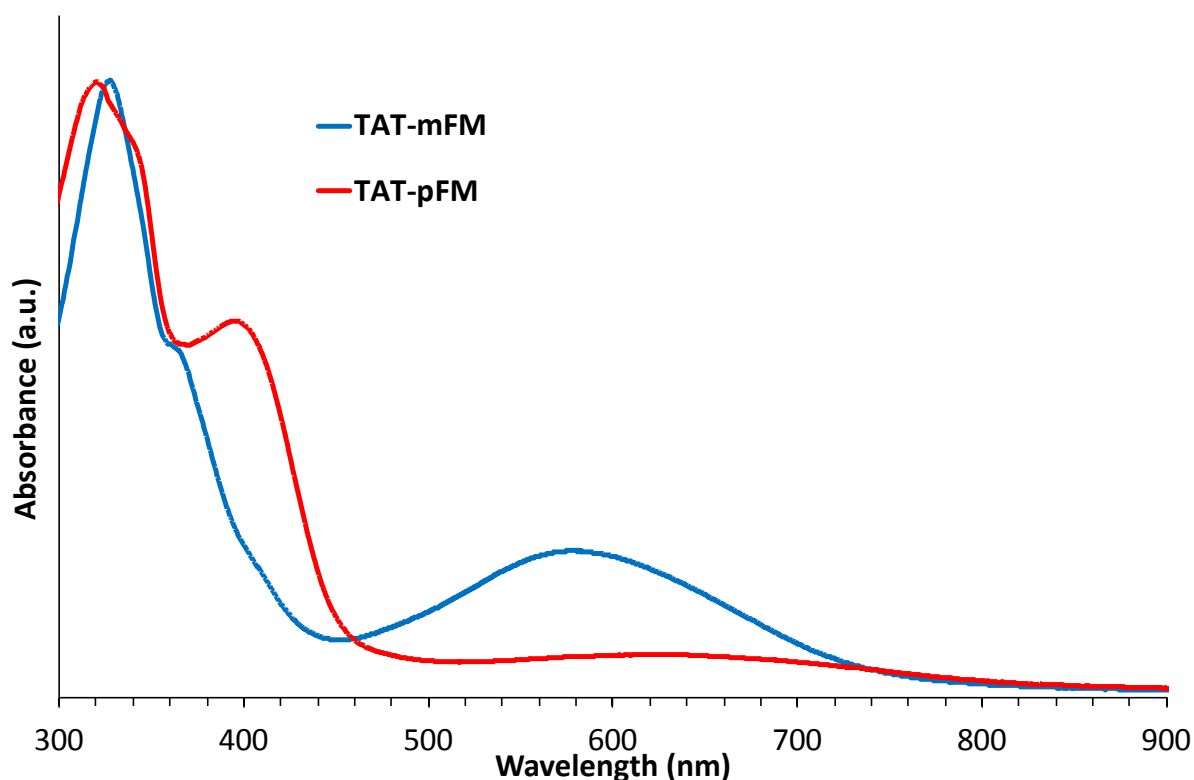


Figure 3. UV-vis spectra in thin-films of TAT-*m*FM (blue) and TAT-*p*FM (red).

The main characteristics of the absorption spectra in solution are found in the solid-state film spectra. However, a slight bathochromic shift of the onset of absorption can be noted for TAT-*m*FM (760 nm) and TAT-*p*FM (890 nm) leading to calculated optical bandgaps, measured from the absorption onsets, of 1.63 eV and 1.39 eV, respectively.

A combination of differential scanning calorimetry (DSC), powder X-Ray diffraction/scattering (PXRD/S) and polarized optical microscopy (POM) allows the comparison of the thermal and structural properties of both molecules. By DSC, TAT-*p*FM exhibits clear melting and crystallization transition peaks at 275°C and 248°C, respectively. However, PXRD/S measurements, combined with POM, clearly highlight the mesomorphic

nature of this dye. Actually, at room temperature, TAT-*p*FM is frozen in a 3D mesomorphic solid state, that gradually flows to a fluid and birefringent mesophase on heating and finally melts into the isotropic liquid at about 270°C (Figure S2). In contrast, TAT-*m*FM is highly crystalline and decomposes before melting above 300°C (Figure S3).

Charge carrier mobilities have been determined by using commercially available bottom-gate/bottom contact (BG/BC) OFETs. The detailed elaboration and characterization procedure of devices can be found in the supporting information (see also Figures S4-S6 for output characteristics). Hole mobility values have been extracted from the linear regime. Data are summarized in the Table 2. The mesomorphic organization in TAT-*p*FM turned to be more favorable for the charge-carrier mobility as this para-derivative exhibits an almost one order of magnitude higher mobility than the crystalline TAT-*m*FM. Overall though, the OFET hole mobilities obtained remain lower than for other previously reported TAT-based dumbbell-shaped molecules.^[14,16] These moderate mobility values are partly attributed to the dicyanomethylene unit which drastically lower the solubility of the dyes and lead to inhomogeneous thin-films.

Table 2. hole mobilities and OPV parameters of TAT-*m*FM and TAT-*p*FM.

	μ_{h^+} (cm ² .V ⁻¹ .s ⁻¹)	V _{oc} (V)	J _{sc} (mA.cm ²)	FF (%)	PCE (%)
TAT- <i>m</i> FM	2.5x10 ⁻⁶	0.95	5.41	38.1	1.95
TAT- <i>p</i> FM	1.5x10 ⁻⁵	0.59	2.99	47.0	0.83

Interestingly, the processing of these two molecules are improved when they are blended with PC₇₁BM in chloroform using diiodooctane (DIO) as an additive. Thus, with more homogeneous thin films, the photovoltaic properties of these new dyes could be investigated in the following reversed configuration: ITO/PEIE/Active layer/MoO_x/Ag. After a careful optimization, we found the best D:A ratio to be 1:1.5 for both molecules. Optimal power conversion efficiencies (PCEs) were found by using DIO as additive in wt% of 0.2 and 0.3% for TAT-*p*FM and TAT-*m*FM, respectively. Despite its lower hole mobility, TAT-*m*FM is the most performing dye of this study with almost 2% of PCE in average (Table 2). Except FF, all photovoltaic parameters are higher for TAT-*m*FM devices (Table 2 and Figure 4). In line with its deeper HOMO level, this dye shows the best V_{oc} with a value as high as 0.95 V. It should be noticed that between the two dyes, the V_{oc} improvement for TAT-*m*FM devices is much higher (0.36 V) than the measured HOMO offset (0.2 eV). This difference may be due to the presence of efficient free-carrier traps in TAT-*p*FM devices that should lower significantly the V_{oc} value compared to the expected one based on the frontier energy-level position. [22,23] This hypothesis is consistent with the current density in TAT-*m*FM devices which is almost twice the one measured for TAT-*p*FM.

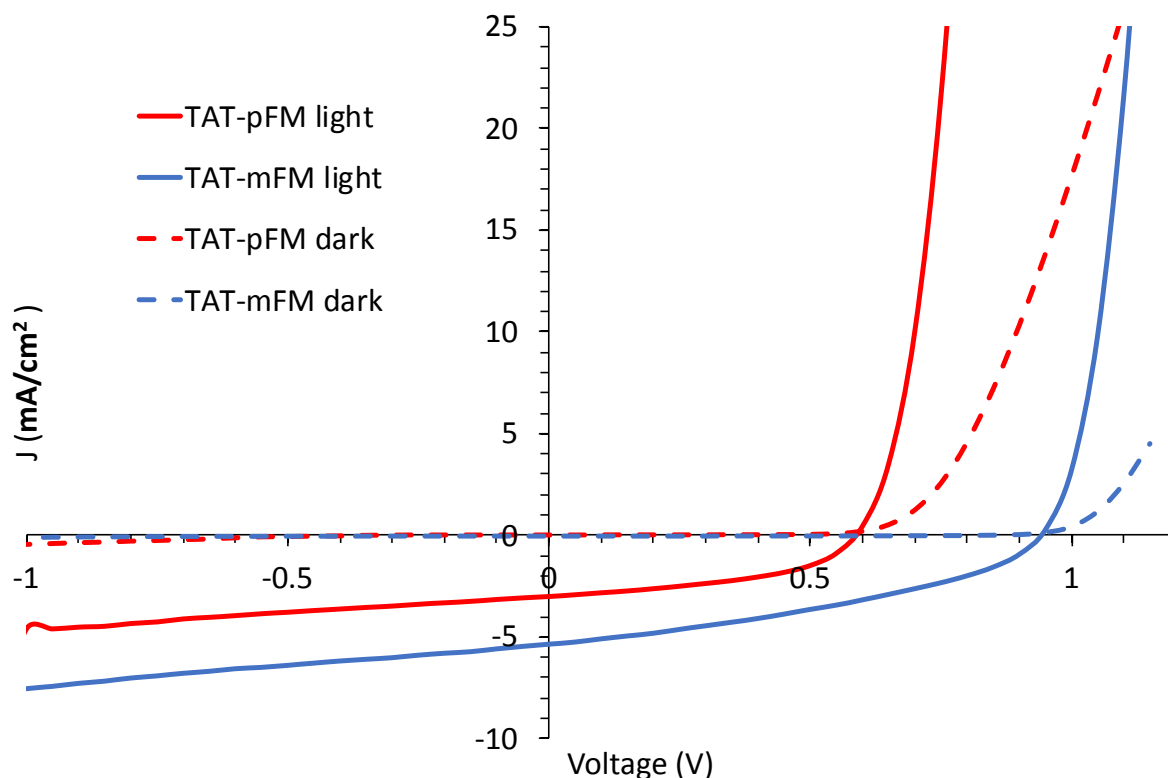


Figure 4. J(V) curves under illumination (full line) and under dark (dashed line) of **TAT-*m*FM** (blue) and **TAT-*p*FM** (red).

This significantly better J_{sc} could also be partly explained by the higher absorbance of the TAT-*m*FM molecule in the ICT range as compared to the TAT-*p*FM dye. In order to validate this point, Figure 5 shows a comparison of the UV-vis absorption spectra of thin films of each of the dyes pure and mixed with PC₇₁BM as well as the EQE spectra measured on organic solar cells. The absorption spectra of the mixtures were measured directly on the previously characterized solar cells. The active layers have the same thickness of about 90-100 nm. Comparison of the absorption spectra of the electron-donor molecules and the mixtures reveals the contribution of PC₇₁BM to the light absorption. Indeed, while the thin films absorption spectrum of TAT-*m*FM and TAT-*p*FM are quite different in solid-state (Figures 3 and 5) the two blend spectra in solid-state are very similar (Figure 5). The difference between the two blends comes from the absorption intensity which is higher for the TAT-*m*FM-based blend between 450 and 650 nm compared to TAT-*p*FM-based blend. This difference is consistent with the position of the ICT absorption band of TAT-*m*FM which overlaps with the absorption of PC₇₁BM in the region between 500 and 700 nm. In the same wavelength-range, TAT-*p*FM hardly absorbs at all. Finally, the EQE clearly show that the charge photogeneration mainly occurs in both blends between 400 and 700 nm. In this area the EQE of the TAT-*m*FM is approximately twice the one of TAT-*p*FM. Considering that both blends have the same PC₇₁BM content and approximately the same thickness, one can conclude that the main difference in between both dyes is originating from the highest ICT absorption band in the TAT-*m*FM material, which contributes significantly to the photocurrent and to the presence of charge-carrier traps in TAT-*p*FM blends that hinder charge-extraction.

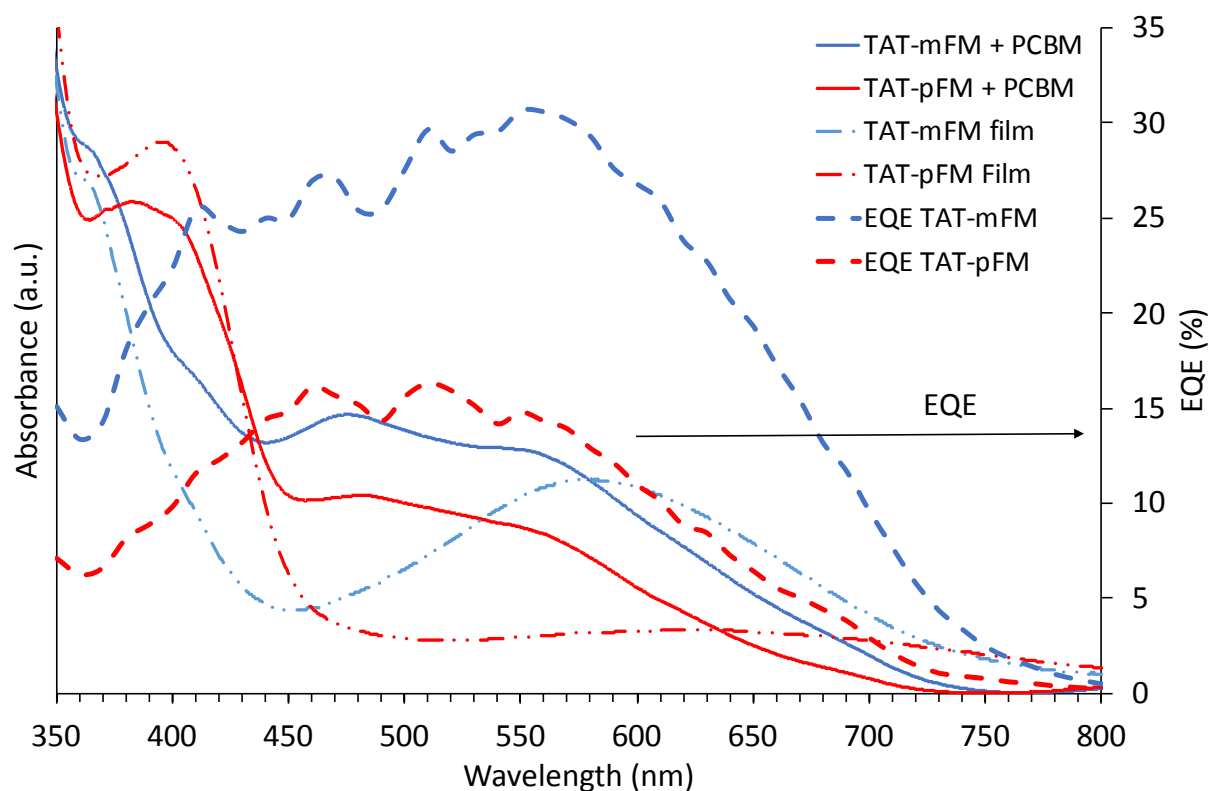


Figure 5. Comparison of absorbance spectra of active layers (full line), pure electron donor dye films (dash and dot line) and EQE (dashed line) for **TAT-*m*FM** (blue) and **TAT-*p*FM** (red).

Conclusion

In summary, two regioisomers of a donor-acceptor-donor (D-A-D) triad have been synthesized and characterized. They are made of two electron-rich triazatruxene (TAT) units connected to a central electron-deficient fluoren-9-ylidene malononitrile (FM) core, via a grafting either at para (2,7-fluorenyl, TAT-*m*FM) or meta (3,6-fluorenyl, TAT-*p*FM) positions. On a first hand, the two regioisomers exhibit different electronic conjugation pathways that drastically affect the absorption properties and energy levels of the molecules. Actually, in this series, the architectural key parameter is the conjugation pathway that connects the TAT donor units to the dicyanomethylene acceptor moiety of the FM core. Thus, in TAT-*m*FM, the meta substitution enables a good conjugation between the donor and acceptor units that exacerbates the ICT band, responsible for the higher absorption, and deepens the HOMO level. TD-DFT calculations are in very good agreement with the experimental data and highlight the strong HOMO-LUMO transition of these ICT bands.

On the other hand, the two regioisomers present quite different structural properties. Thus, while TAT-*p*FM exhibits a stable 3D mesomorphic organization from room-temperature to the melting, TAT-*m*FM remains crystalline and decomposes before melting.

Finally, despite a lower hole mobility, the TAT-*m*FM exhibits the highest PCE of about 2 % essentially from the positive ICT band contribution to the charge photogeneration. Overall, these results contribute to a better understanding of architectural key parameters in such D-A-D dumbbell-shape conjugated molecules, and highlight the often-overlooked influence of regioisomers on optoelectronic properties.

Experimental Section

General Methods.

Synthesis. All reactions were performed under an atmosphere of dried argon using standard Schlenk tube techniques. All chemicals were used as received from commercial sources unless stated otherwise. Chromatographic purifications were performed using silica gel (40–63 μm). TLC was performed on silica gel plates coated with fluorescent indicator.

NMR analysis. ^1H NMR (400 MHz) and ^{13}C NMR (100 MHz) spectra were recorded at room temperature and at high temperatures (90°C) on a Bruker Advance III HD 400 MHz spectrometer.

MALDI-TOF analysis. The mass molar MALDI-TOF spectrometry was given by Bruker Daltonics flex Analysis.

UV-Visible Spectroscopy. Absorption spectra in solution and in thin films were recorded on a Shimadzu UV-2600 spectrophotometer. In solid state, the absorption spectra were measured on thin films drop-casted on glass substrates from a 0.5 mg/mL chloroform solution of organic dyes.

Electrochemical measurements. Cyclic voltammetry (CV) was recorded with a VSP BioLogic potentiostat/galvanostat with a scan rate of 100 mV/s using 0.1 M tetrabutylammonium tetrafluoroborate (Bu_4NBF_4) in CH_2Cl_2 as supporting electrolyte, a Ag/AgCl electrode as the reference electrode, a Pt wire electrode as working electrode, a Pt wire as counter electrode and ferrocene/ferrocenium (Fc/Fc⁺) as a reference. The cell was briefly deoxygenated with argon before each scan.

Differential Scanning Calorimetry. DSC measurements were performed with TA Instruments Q1000 instrument, operated at scan rate of 5°C/min on heating and on cooling.

Thermogravimetric analysis. TGA measurements were carried out on a SDTQ 600 apparatus at scanning rate of 10 °C/min. A differential thermal analysis (DTA) signal was simultaneously measured.

Powder X-Ray diffraction/scattering. PXRD/S measurements were performed with a transmission Guinier-like geometry. A linear focalized monochromatic Cu $K_{\alpha 1}$ beam ($\lambda = 1.5405 \text{ \AA}$) was obtained using a sealed-tube generator (600 W) equipped with a bent quartz monochromator. The samples were filled in 1 mm Lindemann capillaries. The temperature was controlled within $\pm 0.01 \text{ }^\circ\text{C}$ and exposure times were of 5 h (20°C) or 1 h (110°C). The patterns were recorded with a curved Inel CPS120 counter gas-filled detector.

Computational methods. All calculations of the compounds were performed using the Gaussian 09 software package¹ and Gauss View 5.0 molecular visualization program Package.

The theoretical simulations were carried out using density functional theory (DFT) with B3LYP (Becke three-parameter Lee–Yang–Parr) exchange-correlation functional.² 6-31G(d,p) was used as a basis set for all atoms (C, N, H, O). Therefore, in this work, TD-B3LYP method has been used to simulate the electronic absorption spectra and the orbitals molecular. It is important to consider the solvent effect on theoretical calculations when seeking to predict the experimental spectra with a reasonable accuracy. The oscillator strengths and excited state energies were investigated using TD-DFT calculations on the fully DFT optimized geometries.

Organic Field Effect Transistors. Bottom contact bottom gate OFET structures were fabricated using commercially available silicon substrates. Lithographically defined Au (30 nm)/ITO (10 nm) bilayers were used as source and drain electrodes and 230 nm thick SiO_2

layer as a gate dielectric. Channel length and width were $L = 20 \mu\text{m}$ and $W = 10 \mu\text{m}$, respectively. Substrates were cleaned consecutively in ultrasonic baths at 45°C for 15 min each step using soapsuds, acetone, and isopropanol and followed by 15 min UV-ozone treatment. Then substrates were transferred into a nitrogen filled glove box where hexamethyldisilazane (HMDS) was spincoated on top of the SiO_2 followed by annealing at 135°C for 10 min. Finally, solutions of pure TAT-*m*FM and TAT-*p*FM were spincoated substrates to complete the FET devices. For each molecule, a concentration of 4 mg/mL in CHCl_3 was used. Prior to characterization, completed devices were dried under high vacuum ($\approx 10^{-5}$ - 10^{-6} mbar). Transistor output and transfer characteristics were measured using a Keithley 4200 semiconductor characterization system. Hole mobilities were extracted in the linear regime using a standard device model.

Organic Photovoltaic devices. ITO coated glass substrates were cleaned in ultrasonic bath of deionized water, acetone and 2-propanol at 45°C for 15 minutes for each step. Then, they were dried by nitrogen and were treated in a UV/Ozone oven to remove residual organic contaminants. PEIE ($M_w = 70000 \text{ g/mol}$) was spin coated (5000 rpm, 60s) to obtain a 5 nm thick layer and thermally annealed for 10 minutes at 100°C under nitrogen atmosphere. The photoactive layer was prepared from different solutions containing TAT-based dye:PC₇₁BM blends with a TAT-based dye concentration of 5 mg/ml in CHCl_3 . The ratio of donor and acceptor was varied from 1:1 to 1:3. The solution were spin-coated onto the PEIE/ITO substrates, and the resulting films were annealed at 120°C for 10 min under a nitrogen atmosphere. The 7 nm thick MoO_3 and 120 nm thick Ag layers were thermally evaporated (Pressure $\approx 1 \times 10^{-6}$ mbar). The effective area of each cell was 12 mm^2 .

OPV measurements. The (J-V) curves of the OPV devices were measured under AM 1.5G-100 mW/cm^2 simulated sunlight irradiation. (J-V) characteristic measurements of photovoltaic devices were conducted using LabView-controlled Keithley 2400 SMU. The performance of solar cells under the dark and illumination were measured using a BET Technologies Sun 3000 solar simulator with an AM1.5G filter. All the photovoltaic parameters of solar devices (V_{OC} , J_{SC} , FF and PCE) were extracted using the LabView software.

Acknowledgements

This work has been supported by the Interreg IV-A program under Rhin-Solar project (nr C25) and the French National Research Agency (ANR ORION project ANR-13-PRGE-0001).

Conflict of interest

The authors declare no conflict of interest.

Keywords: Organic semiconductor • regioisomer • absorption spectroscopy • solar cells • triazatruxene

References

- [1] C. Cui, Y. Li, *Energy Environ. Sci.* **2019**, *12*, 3225-3246.

- [2] M. Lindorf, K. A. Mazzi, J. Pflaum, K. Nielsch, W. Brütting, M. Albrecht, *J. Mater. Chem. A* **2020**, *8*, 7495-7507.
- [3] C. Yan, S. Barlow, Z. Wang, H. Yan, A. K.-Y. Jen, S. R. Marder, X. Zhan, *Nature Reviews* **2018**, *3*, 18003.
- [4] N. Leclerc, P. Chávez, O. A. Ibraikulov, T. Heiser, P. Lévêque, *Polymers* **2016**, *8*, 11.
- [5] F. Lincker, A.-J. Attias, F. Mathevet, B. Heinrich, B. Donnio, J.-L. Fave, P. Rannou, R. Demadrille, *Chem. Commun.* **2012**, *48*, 3209-3211.
- [6] L. Sicard, C. Quinton, J.-D. Peltier, D. Tondelier, B. Geffroy, Urelle Biapo, R. Métivier, O. Jeannin, J. Rault-Berthelot, C. Poriel, *Chem. Eur. J.* **2017**, *23*, 7719-7727.
- [6'] C. Poriel, L. Sicard, J. Rault-Berthelot, *Chem. Comm.* **2019**, *55*, 14238-14254.
- [6 «] J.-D. Peltier, B. Heinrich, B. Donnio, O. Jeannin, J. Rault-Berthelot, C. Poriel, *Chem. Eur. J.*, **2017**, *23*, 17290-17303.
- [7] I. Bulut, P. Chávez, S. Fall, S. Méry, B. Heinrich, J. Rault-Berthelot, C. Poriel, P. Lévêque, N. Leclerc, *RSC Advances* **2016**, *6*, 25952-25959.
- [8] X. Zhou, Q. Sun, W. Li, Y. Zhao, Z. Luo, F. Zhang, C. Yang, *Dyes and Pigments* **2017**, *146*, 151-158.
- [9] R. Singh, G. Pagona, V. G. Gregoriou, N. Tagmatarchis, D. Toliopoulos, Y. Han, Z. Fei, A. Katsouras, A. Avgeropoulos, T. D. Anthopoulos, M. Heeney, P. E. Keivanidis, C. L. Chochos, *Polym. Chem.* **2015**, *6*, 3098-3109.
- [10] R. Rieger, D. Beckmann, A. Mavrinskiy, M. Kastler, K. Müllen, *Chem. Mater.* **2010**, *22*, 5314.
- [11] I. McCulloch, M. Heeney, M. L. Chabinyc, D. DeLongchamp, R. Joseph Kline, M. Cölle, W. Duffy, D. Fischer, D. Gundlach, B. Hamadani, R. Hamilton, L. Richter, A. Salleo, M. Shkunov, D. Sparrowe, S. Tierney, W. Zhang, *Adv. Mater.* **2009**, *21*, 1091-1109.
- [12] B. Jia, M. Li, J. Zhou, Y. Xiao, S. Zhang, J. Wang, X. Lu, Z. Xie, Z. Tang, X. Zhan, *Chem. Mater.* **2021**, *33*, 441-451.
- [13] I. Bulut, P. Lévêque, B. Heinrich, T. Heiser, R. Bechara, N. Zimmermann, S. Méry, R. Ziessel, N. Leclerc, *J. Mater. Chem. A* **2015**, *3*, 6620-6628.
- [14] I. Bulut, P. Chávez, A. Mirloup, Q. Huaultmé, B. Heinrich, A. Hébraud, S. Méry, R. Ziessel, T. Heiser, P. Lévêque and N. Leclerc, *J. Mater. Chem. C* **2016**, *4*, 4296-4303.
- [15] I. Bulut, Q. Huaultmé, A. Mirloup, P. Chávez, S. Fall, A. Hébraud, S. Méry, B. Heinrich, T. Heiser, P. Lévêque, N. Leclerc, *ChemSusChem* **2017**, *10*, 1878-1882.
- [16] T. Han, I. Bulut, S. Méry, B. Heinrich, P. Lévêque, N. Leclerc, T. Heiser, *J. Mater. Chem. C* **2017**, *5*, 10794-10800.
- [17] L. D. Pham, L. Gil-Escrig, K. Feron, S. Manzhos, S. Albrecht, H. J. Bolink, P. Sonar, *J. Mater. Chem. A* **2019**, *7*, 12507-12517.
- [18] L. A. Estrada, D. C. Neckers, *J. Org. Chem* **2009**, *74*, 8484-8487.
- [19] F. Bigi, M. L. Conforti, R. Maggi, A. Piccinno, G. Sartori, *Green Chem.*, **2000**, *2*, 101-103.
- [20] C. J. Tonzola, A. Babel, S. A. Jenekhe, *Chem. Mater.* **2004**, *16*, 4556-4573.
- [21] L. A. Estrada, X. Cai, D. C. Neckers, *J. Phys. Chem. A* **2011**, *115*, 2184-2195.
- [22] M. C. Scharber, *Adv. Mater.* **2016**, *28*, 1994-2001.
- [23] A. Chelouche, G. Magnifouet, A. Al Ahmad, N. Leclerc, T. Heiser, P. Lévêque, *J. Appl. Phys.* **2016**, *120*, 225501